Article

Analyzing Dynamical Disorder for Charge Transport in Organic Semiconductors via Machine Learning

Patrick Reiser, Manuel Konrad, Artem Fediai, Salvador Léon, Wolfgang Wenzel, and Pascal Friederich*

Read Online

ACCESS | Metrics & More | Article Recommendations | Supporting Information

ABSTRACT: Organic semiconductors are indispensable for today's display technologies in the form of organic light-emitting diodes (OLEDs) and further optoelectronic applications. However, organic materials do not reach the same charge carrier mobility as inorganic semiconductors, limiting the efficiency of devices. To find or even design new organic semiconductors with higher charge carrier mobility, computational approaches, in particular multiscale models, are becoming increasingly important. However, such models are computationally very costly, especially when large systems and long timescales are required, which is the case to compute static and dynamic energy disorder, *i.e.*, the dominant factor to determine charge transport. Here, we overcome this drawback by integrating machine learning models into multiscale simulations. This allows us to obtain unprecedented insight into relevant microscopic materials properties, in particular static and dynamic disorder contributions for a series of application-relevant molecules. We find that static disorder and thus the distribution of shallow traps are highly asymmetrical for many materials, impacting widely considered Gaussian disorder models. We furthermore analyze characteristic energy level fluctuation times and compare them to typical hopping rates to evaluate the importance of dynamic disorder for charge transport. We hope that our findings will significantly improve the accuracy of computational methods used to predict application-relevant materials properties of organic semiconductors and thus make these methods applicable for virtual materials design.
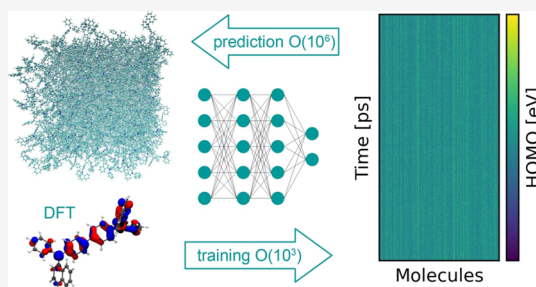
INTRODUCTION

Motivation. Organic semiconductors have been successfully integrated into many commercially relevant electronic devices such as in organic light-emitting diodes (OLEDs),[1] organic photovoltaics (OPV),[2] organic lasers,[3] and organic transistors (OFETs).[4] Their optoelectronic properties and potential flexibility, role-to-role manufacturing,[5] or biocompatibility[6] open many interesting applications. However, concerning charge carrier transport and mobility, organic semiconductors still fall short behind their inorganic counterparts. Electrochemical doping of organic semiconductors significantly increases conductivity as well as charge carrier injection but can reduce long-term stability and efficiency due to drift and diffusion of dopants.[7−10] Although organic crystals achieve high mobilities in the range of 1−100 cm²/(V s),[11,12] they are usually not used in OLEDs. An OLED made from a single crystalline layer will likely suffer from charge carrier injection and recombination imbalances.[13] To achieve isotropic light emission and homogeneous layer thickness in device stacks with multiple layers, amorphous or semicrystalline materials are required, having significantly lower charge carrier mobilities. Consequently, it is crucial to understand and to improve charge transport, in particular charge mobility, for common OLED and OPV materials, which is determined primarily by the width of the disorder distribution, as shown by Bässler and Köhler.[14−16] The enormous suppression of the

mobility with increasing disorder is largely responsible for the poor performance of amorphous organic semiconductors with respect to mobility. Multiscale modeling methods had large success in *ab initio* mobility prediction for various materials and therefore serve as a screening tool for new or modified molecules.[7,17−24] In most of the models, charge transport is described as a sequence of hopping processes, *i.e.*, thermally assisted tunneling of localized polarons between neighboring molecules.[25] Hopping rates can be estimated based on the Miller−Abrahams model and Marcus theory,[26,27] which require reorganization energies and transition matrix elements from *ab initio* DFT calculations, as well as the spatial distribution of molecular energy levels. The hopping rates can then be inserted into master equations,[28−30] Monte Carlo simulations,[31] or mean field theories[32] to determine the carrier mobility of interest.[33,34]

Presently, most of the quantitative models for the mobility assume a static picture with frozen molecules and thus time-

Scheme 1. Molecules[a]
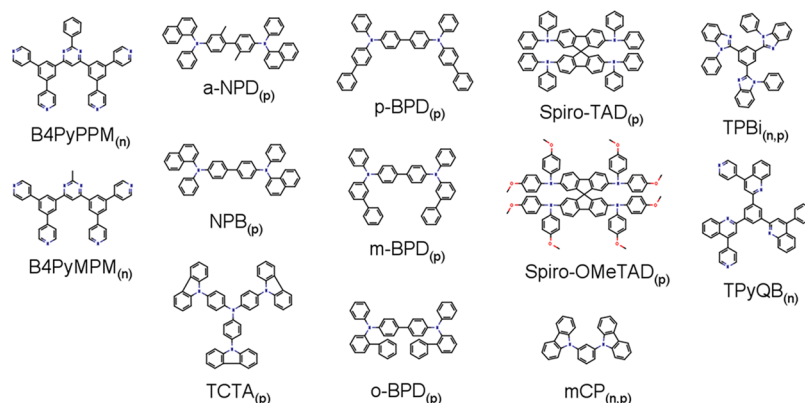
[a]Structure for all molecules investigated in this study. They can be categorized into p-type and n-type semiconductors. P-type: α-NPD, NPB, Spiro-TAD, Spiro-OMeTAD, TCTA, BPD, and mCP. N-type: B4PyPPM, B4PyMPM, TPBi, and TPyQB.

independent energy levels, although molecular morphologies are often created by dynamics simulations.[21,35,36] This is partly due to the numerical effort of electronic structure methods, such as DFT, which precludes their use in large systems with full dynamics. For this reason, the role of dynamic disorder is presently not well-understood.

Static and Dynamic Disorder. In amorphous molecular solids, at any given point in time, the distribution of orbital energies across all molecules in the system is typically estimated to be Gaussian with a material-dependent standard deviation, which is referred to as (global) energy disorder in the Gaussian disorder model.[14] The disorder parameter σ constitutes a sensitive factor for mobility prediction: $\mu \propto e^{-C(\sigma/kT)^2}$. However, due to thermal vibrations around the individual (and potentially different) equilibrium conformations of each molecule in the amorphous matrix, these energy levels are fluctuating in time. The thermally driven conformational disorder can include methyl rotations,[37] pedal motions,[38] resonances in hydrogen bonds,[39] or dipole orientational[40] disorder.[41,42] This fluctuation is referred to as dynamic disorder,[43−45] which is related to electron−phonon interactions, which cause a spread of energy levels. If all molecules had the same equilibrium conformation, all time-averaged energy levels would be equal. However, in most of the amorphous materials, the molecules are constrained in individual equilibrium structures, leading to a spread of the time-averaged energy levels, which is referred to as static disorder.[46] It will depend on the size and flexibility of the molecules, on the response of energy levels to conformational changes, on the degree of crystallinity, and on possible additives such as dopants.[47] The effective energy landscape and energy disorder experienced by the charge carriers thus depend on the typical residence time of charge carriers,[48,49] i.e., electrons and holes localized on a single molecule. In case that the residence time is much smaller than the fluctuation time of energy levels (high electronic coupling between molecules), the dynamic disorder has to be taken into account, and the total disorder becomes an upper bound of the energy disorder. However, in case of lower hopping rates, each charge carrier will experience a fluctuating energy landscape potentially with multiple resonances with neighboring energy levels, leaving the static disorder as a lower bound.[48] As a consequence, the thermal energy fluctuations and the resulting dynamic disorder can be beneficial or detrimental to charge transport. This will

depend on whether the charge transport is limited by either static disorder or electronic couplings between neighboring molecules, where the transfer integral is influenced by orientation and distance as well. Additionally, electrostatic interaction will modify the energy landscape, as soon as a charge is moving in the system. Depending on the transport model, the energy distribution integrated over in percolation path theory for mobility prediction or used in Monte Carlo simulations to initialize site energies is often assumed to be static. However, the disorder is commonly estimated by the total disorder, or the morphologies are generated by dynamics simulations only, because of the computational cost of energy calculations.[21,33,35,36,50]

Therefore, we incorporated faster machine learning (ML)[51] models to upscale energy predictions on long trajectories with thousands of molecules in order to obtain insights into the dynamics of disorder effects and to distinguish static and dynamic disorder contributions.[43,44,52−54]

This Work. In a recent proof of principle study, we showed that energy level fluctuations in PEDOT:PSS can be evaluated using machine learning models, enabling the calculation of dynamic and static disorder in PEDOT oligomers.[55] In this paper, we present an extended study of static and dynamic disorder, evaluated using ML models for OLED and OPV application-relevant materials (depicted in Scheme 1). For this study, we focus on conformational disorder and evaluate vacuum single-point energies for isolated molecules from DFT reference calculations to train the ML models. Electrostatic disorder due to the electrostatic potential of neighboring molecules as well as additional electrons and holes is neglected here but plays an important role to quantify charge carrier mobility in amorphous organic semiconductors.[21,34,56] We show that machine learning models can be trained to reliably predict orbital energies with a limited number of DFT calculations and subsequently used to compute static and dynamic disorder on the full set of MD trajectories. Thereby, we obtain good statistics for a comprehensive analysis of energy disorder as a function of time and position. This enables us to compare dynamic energy changes between neighboring molecules with typical hopping rates of charge carriers. In this work, we have succeeded in separating the static disorder from the dynamic disorder, which is often larger than the former. The comparison of hopping and energy level fluctuation rates is required to verify the static disorder being
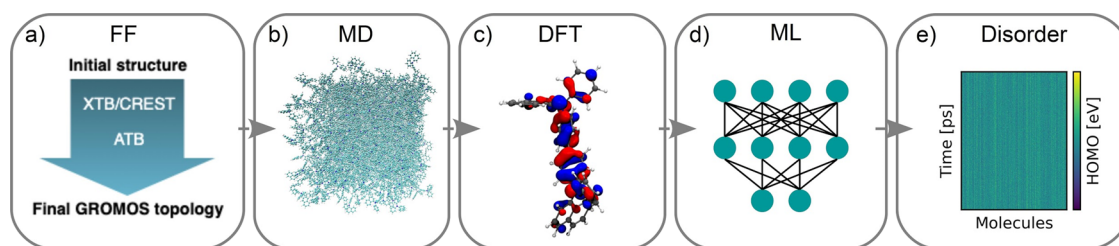
Figure 1. Computational workflow. The full workflow can be divided into (a) conformer search and force field parameterization (FF), (b) molecular dynamics simulation (MD), (c) density functional theory (DFT) calculations, (d) machine learning model (ML) generation, and (f) final energetics analysis of the full trajectories to estimate disorder.

used for multiscale models. Nonetheless, we discuss that for a certain parameter range, the dynamic disorder could become relevant to more accurately predict the charge carrier mobility of amorphous organic semiconductors. We expect that our method will enable accurate prediction of the charge carrier mobility in amorphous organic semiconductors, paving the way to a reliable virtual design of high-mobility amorphous organic semiconductors.

METHODS

The workflow used in this study consists of the parameterization of molecule-specific classical force fields (FF), molecular dynamics simulations (MD) of the amorphous solid, DFT calculations on individual snapshots to generate a sufficiently large dataset of HOMO energy levels, training of machine learning models, in particular neural networks (NN), to predict energy levels as a function of the conformation of a molecule, and finally energetics prediction on the full MD trajectories using the ML model instead of expensive DFT calculations. The individual steps of the workflow are depicted in a schematic overview of Figure 1. In the following, we will give information on each step and their mutual relation. With this procedure, all molecules in Scheme 1 have been investigated.

Molecular Dynamics. For each molecule, the geometry is initially optimized with a conformer search using the submodule CREST of the semiempirical program package XTB[57−59] to find the minimum energy conformation. The resulting structure is submitted to the online platform ATB,[60,61] which automatically assigns GROMOS force field parameters and partial charges.[62] For the simulation of the melt structures, we use the molecular dynamics (MD) code LAMMPS.[63] Throughout this work, we use a time step of 1 fs and a cutoff of 14 Å for short-range interactions in combination with the PPPM long-range solver for electrostatics and Nosé−Hoover style thermostating and barostating. The MD simulation is initialized by placing randomly rotated molecules on a grid followed by a cascade of NPT runs to equilibrate the density. During an initial pressure ramp from 10 to 1 atm and at a temperature of 300 K, the loose initial structure is condensed into a solid over a period of 200 ps. Then, the long-range solver is activated followed by an additional run of 200 ps at the final pressure of 1 atm. In order to further equilibrate the density, the system is heated from 300 to 700 K and subsequently cooled back to 300 K, in each case as linear ramps of 200 ps. At the final conditions of 300 K and 1 atm, the system is equilibrated for another 500 ps. Finally, in the production runs, we extract snapshots in an interval of 1 ps over a period of 5 ns and in an interval of 1 fs over a period of 1 ps. A typical example for the development of

the mass density during the equilibration and production runs is shown in Figure S13 of the Supporting Information.

DFT. In order to generate a suitable conformer-energy dataset to train machine learning models, we performed density functional theory (DFT) calculations with the Turbomole 7.4 software package on randomly sampled conformers.[64] We used the resolution of identity approximation with a def2-SV(P) basis set on an M3 grid and the B3-LYP functional.[65] We extracted the total energy as well as vacuum HOMO and LUMO energy levels from DFT single-point energy calculations. We simply used the last 20−100 snapshots of the MD trajectories with large time steps, which leads to a set of less correlated conformers compared to the trajectories with a smaller time step. Each snapshot has 512 molecules (mCP has 1000 molecules), which leads to approximately 10,000−50,000 conformers and corresponding energy levels of each material for training. Additionally, we randomly picked 6 molecules in each simulation box and calculated DFT energies for the full trajectories from 0 to 5000 ps with a total of approximately 30,000 conformational energies, which serves as an additional test set and to estimate approximate DFT-based disorder values. Moreover, we calculated energy levels using DFT along 6 trajectories for the small time step MD trajectories of randomly selected molecules. We further experimented with different basis set and grid options (see the Supporting Information for details). There is a small dependence of the DFT results on the basis set size, which likely improves going to def2-TZVP and def2-QZVP, at the cost of a significant increase in computational effort, which makes a DFT reference uncertainty of a few meV seem acceptable.

ML. For our machine learning model, we chose a fully connected feed-forward neural network (NN) of 3 layers with a leaky RELU activation function ($\alpha = 0.05$) followed by a single linear classification layer. We trained a separate NN for each material on the respective DFT energy dataset generated in the previous step. As input features, we used rotationally invariant, geometry-derived descriptors, such as inverse distances and bond and dihedral angles. Because of the large size of some organic semiconductors in this study, we further restricted the number of inverse distances to a set of close neighbors per atom (including hydrogens). The input features were subsequently concatenated and standardized. The NNs were trained using the Adam optimizer with a learning rate decreasing from 5×10^{-4} to 1×10^{-5} over 400 epochs. We found a good convergence for a broad set of hyperparameters and selected an NN with 3 hidden layers of 1000 neurons before the final regression layer. To prevent overfitting, we applied L1 regularization for kernel and bias ($10^{-6}−10^{-7}$). Note, an exhaustive hyperparameter optimization was not
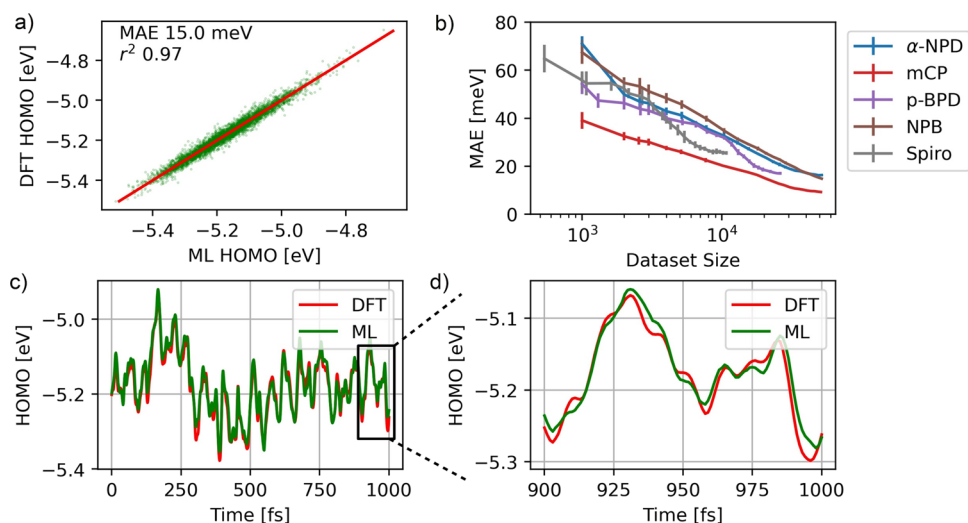
Figure 2. Machine learning. We trained an NN for all molecules in Scheme 1 to predict HOMO and LUMO levels. (a) Scatterplot of DFT reference values versus the predicted validation set for NPB. (c) Validation trajectory comparing the DFT reference with ML-predicted trajectory for NPB. (b) Learning curve for NPD, *p*-BPD, NPB, Spiro-TAD, and mCP, which shows the mean absolute error (MAE) as a function of training data for a 10-fold cross-validation. (d) Zoom into an oscillation of (b).
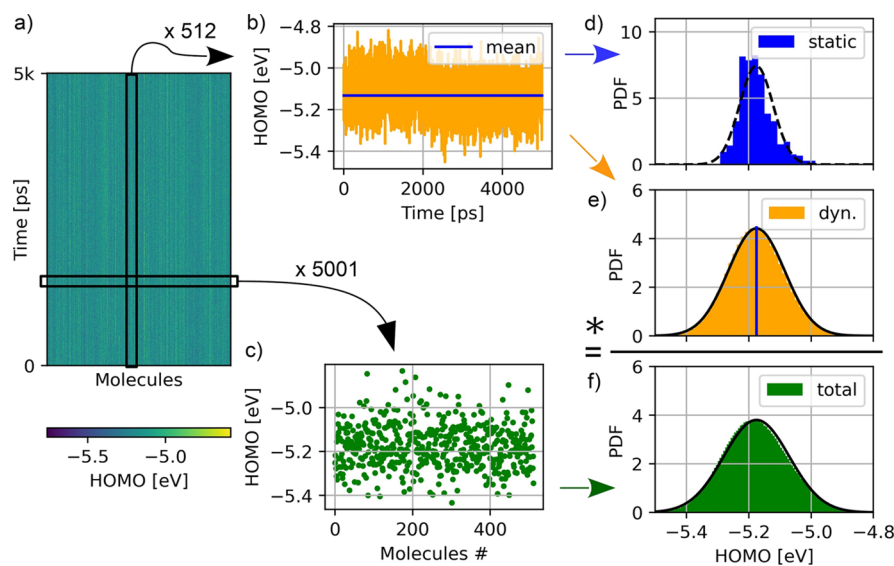

Figure 3. Definition of disorder. The analysis of static and dynamic energy disorder is illustrated by the example of NPB. (a) Heat map of all NN predictions, where time flows in the *y*-direction. (b) One out of 512 trajectories. (c) Single snapshot out of 5001 at a specific time showing all molecules. (d) Probability density function (PDF) plot of the distribution of all the trajectories' mean value representing the static disorder distribution. (e) Dynamic contribution of the trajectories. The fluctuations of all trajectories centered to their respective mean value. (f) Total conformational disorder distribution from averaged snapshots, which is composed of a convolution of the static and dynamic distributions, *i.e.*, the squared sum of dynamic and static disorder.

found to be necessary, which is why only the regularization parameters were tuned. For evaluation, we choose a validation training set split ratio of 0.1.

Dynamic Disorder. As mentioned in the Introduction, the conformational energy disorder of molecular solids has dynamic and static contributions. Combined with electrostatic contributions, which are described in more detail in prior work,[21,34,66] they add up to the total distribution of energy levels. Provided that the energy $U_i(t)$ is given for each molecule i at every point in time by our ML model, the conformational disorder components can be separated as shown in Figure 3. This is done by evaluating either the variance of energy levels for a single molecule with time or the distribution of time-averaged energies within the ensemble.

The dynamic disorder is characterized by the expectation value of the variance of energy fluctuations of each molecule with time

$$\sigma_d^2 = E_i[\text{Var}_t[U_i(t)]] \tag{1}$$

Here, $\text{Var}_{t/i}$ represents the variance and $E_{t/i}$ denotes the expectation value with respect to time t or ensemble average i, respectively. Correspondingly, the static disorder is defined by the variance of the time-averaged expectation values of the energy levels of each molecule

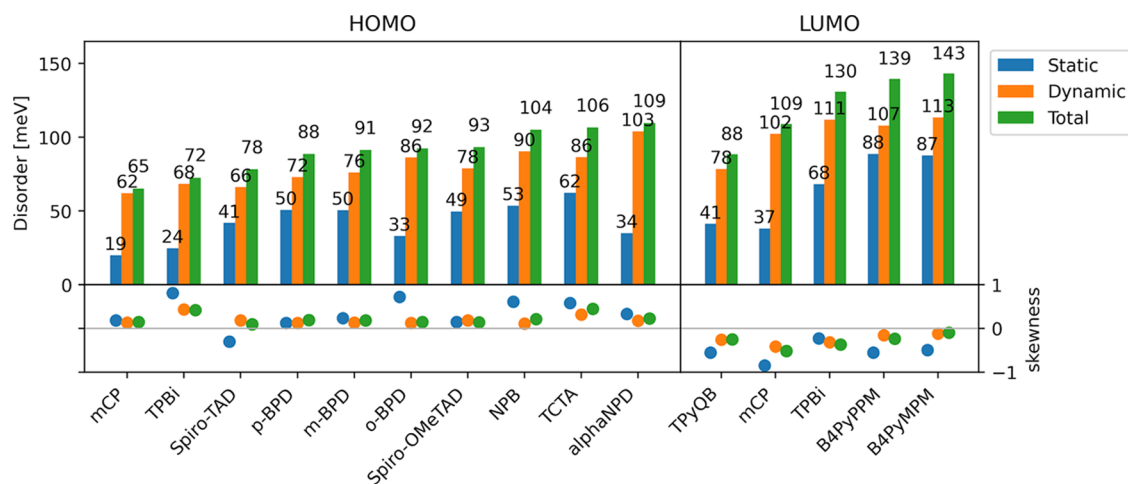$$\sigma_s^2 = \text{Var}_i[E_t[U_i(t)]] \tag{2}$$

Figure 4. Disorder components and (a)symmetry. Energy disorder broken down into dynamic and static parts as illustrated in Figure 3. The LUMO level for all n-type molecules and the HOMO level for all p-type molecules are plotted (see Scheme 1). All 38.3 million energy levels required for this analysis are generated by our machine learning models. All ML estimates of HOMO and LUMO disorder are given in Tables S3 and S4 and Figures S8 and S9. The corresponding values obtained from DFT reference trajectories with significantly smaller statistics are given in Tables S1 and S2 for comparison. The lower panels show a measure of skewness of the static, dynamic, and total energy level distributions. In particular, for the static energy level distributions, we find substantial deviations from symmetrical Gaussian distributions.

If both distributions can be approximated independently by normal distributions, then the total conformational disorder $\sigma_t^2 = \mathrm{Var}_{i,t}[U(t)]$ is given by the quadratic sum of dynamic and static disorder

$$\sigma_t^2 = \sigma_d^2 + \sigma_s^2 \qquad (3)$$

We note that in the following discussion, we neglect the electrostatic contribution[56] and focus solely on conformational disorder.

RESULTS AND DISCUSSION

We trained our machine learning model on the DFT-generated HOMO-conformer dataset for each relevant molecule in Figure 2. HOMO/LUMO energy levels are used here as a proxy for the IP/EA levels, which are relevant for charge transport. However, as we do not take polarization effects into account, explicit polarons and thus IP/EA levels are not required in this discussion. The dependence on the number of training samples can be seen from the learning curve in Figure 2b, yielding an exponential reduction of the mean absolute validation error on the training set size. For all molecules, a validation error of 1 kcal/mol or lower is achieved with 10,000 random conformers from the large time step trajectories. The ML-predicted HOMO energies are plotted versus the ground truth of the DFT HOMO levels in a scatterplot for NPB in Figure 2a. Here, we achieve a mean absolute error (MAE) of 15 meV with an r^2 score of 0.97, which is well below chemical precision and the estimated disorder values. We find that NNs trained on ensembles of molecules from only a few snapshots as for NPB nicely generalize the test trajectories of single molecules for longer timescales (r^2 score of 0.96). However, the opposite is not true as NNs trained solely on a few trajectories do not correctly predict other trajectories or snapshots (for NPB, only an r^2 score of 0.6). This is most likely due to the fact that for a single trajectory, all reachable dynamic conformations are confined around their positional dependent mean and do not visit the full conformational space. The models trained on random snapshots from the large time step dataset adequately predict the small time step trajectory,

which is depicted in Figure 2c for NPB. The small time step MD simulation is used to investigate oscillations and hopping timescales in Figure 5.

Applying the trained machine learning model on the full MD trajectories, all conformational energies are predicted, illustrated in Figure 3a with NPB as an example. Looking at snapshots in Figure 3c, i.e., at all molecules at a specific time, the total conformational disorder can be determined based on the HOMO level distribution and its standard deviation in Figure 3f. The total conformational disorder is approximately Gaussian. The HOMO and LUMO level distribution for all molecules is further evaluated directly from DFT reference calculations in Figures S1 and S2. Although the total conformational disorder can be directly inferred from DFT data, a distinction between static and dynamic contributions requires complete trajectories as in Figure 3b. In the image of Figure 3a, trajectories can be seen as vertical slices along the time axis. The distribution of their mean values is plotted in blue in Figure 3d, whereas the scattering around their respective mean values is depicted in Figure 3e. Importantly, the machine learning model provides enough trajectories to properly represent the distribution of time-averaged energy levels and their fluctuations. Therefore, the standard deviation of the distributions in Figure 3d and Figure 3e can be taken as an estimate for the static and dynamic disorder following eqs 2 and 1, respectively. Additionally, we approximated the static and dynamic disorder based on DFT reference values from six test trajectories in Tables S1 and S2.

Following this data analysis, we determine disorder components for the HOMO level of all p-type molecules and for the LUMO level of all n-type molecules in Scheme 1. The individual disorder values are depicted in Figure 4 and listed in Tables S3 and S4 together with the ML validation error and the squared sum of dynamic and static disorder. We find an overall very good agreement of the squared sum with the total conformational disorder value, showing that the disorder is composed of a convolution of independent dynamic and static disorder contributions, which cannot be concluded
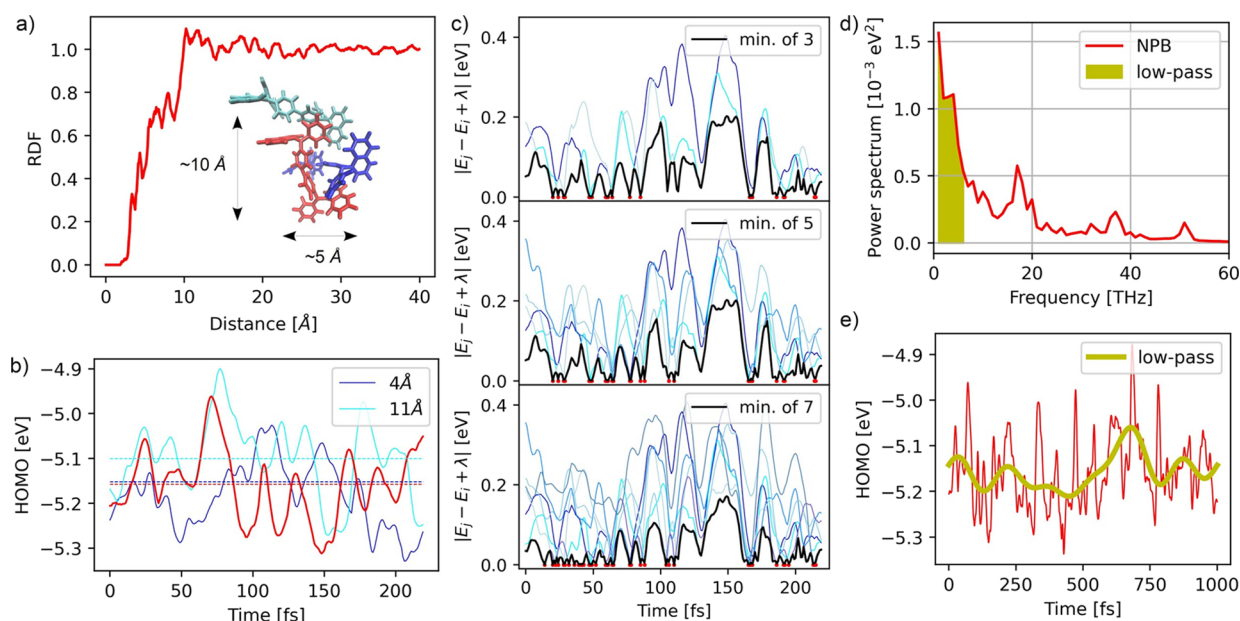
Figure 5. Hopping rate and energy matching. (a) Radial distribution or pair correlation function for NPB obtained from averaged MD morphology. The inset shows the stacking of NPB molecules in the amorphous phase with two common length scales as an example arrangement. (b) ML prediction of energies of a random NPB molecule (red) and selected neighboring molecules in blue and cyan at ca. 4 and 11 Å distance. (c) Absolute energy differences, including reorganization energy λ, of the central molecule to the 3, 5, and 7 nearest neighbors in shades of blue and their minimum in black and resonances in red. (d) Averaged power spectrum of NPB from FFT of ML-predicted trajectories. (e) Trajectory of the molecule in (b) with low-pass filtered frequency components in orange.

from the six DFT reference trajectories alone due to limited statistics.

In general, we find a notable contribution of the dynamic part to the total conformational disorder. As discussed later, the dynamic disorder has the potential to hinder charge transport.[67] The static disorder seems to be larger for molecules with long rotatable aromatic groups such as TCTA, where the vacuum HOMO level is delocalized and can localize inside groups depending on the conformation (see Figure S5). Also, in direct comparison of *m*-BPD and *p*-BPD with *o*-BPD, the more compact and sterically locked ortho position shows the smallest static disorder. Similarly, with the addition of methyl groups in the backbone of NPB (yielding α-NPD), static disorder decreases, and the ratio between static and dynamic disorder is altered. However, the reduction in static disorder of methyl-substituted α-NPD is compensated by an increase in dynamic disorder.

While the total and dynamic disorder can be well-described with a Gaussian distribution, the static disorder is often slightly asymmetric (see Figure 3b, the lower panel in Figure 4, and the Supporting Information). Electrons and holes with hopping rates that are lower than the typical fluctuation time of the dynamic disorder will thus experience an asymmetrical distribution of energy levels. Depending on the type of asymmetry, this might lead to a decrease or increase in the concentration of tail states/shallow traps. In the example illustrated in Figure 3d, the holes traveling through NPB are in a skewed HOMO distribution that shows more tail states and thus hole traps than what would be expected from a Gaussian distribution of energy levels with the same standard deviation. The opposite behavior was observed in Friederich et al.[55] for hole transport in PEDOT oligomers, where the distribution of HOMO levels showed an extended tail toward lower HOMO energy levels and a sharp edge toward more shallow HOMO energies. One possible explanation of this behavior might be

the correlation between total energy and HOMO energy close to the equilibrium conformation. In case of a positive correlation, the HOMO distribution has a global minimum, leading to a distribution as shown in Figure 3d, whereas in case of a negative correlation, the opposite asymmetry is observed. This can be seen in the example of PEDOT and in various cases in Figure 4, especially for distributions of static LUMO energy levels and for the distribution of static HOMO energy levels of Spiro-TAD.

Depending on the theoretical model used to describe charge transport, also, the structurally resolved energy levels of the surroundings of a molecule can be required. For example, in kinetic Monte Carlo simulations, charge transport is modeled as stochastic charge transfer between different sites subject to an external electric field. With our machine learning model, the time-resolved energetic neighborhood to a molecule can be explored.

In the following, we will analyze the time-resolved energy difference between neighboring molecules at the examples of a small NPB cluster and compare it to typical hopping rates. The power spectrum of the energy level fluctuations of NBP molecules (see Figure 5d) shows an approximate $1/f$ noise-like background, reaching down to a few THz. In addition, we find distinct vibrational modes leading to oscillations with a frequency of ~17 THz (59 fs), which corresponds to the more pronounced oscillations plotted in Figure 5b. Furthermore, we find additional frequency components at ~37 and ~51 THz (59 and 27 fs, respectively), corresponding to weaker fluctuations that are modulated on the main fluctuations in Figure 5b. The frequency of energy level resonances (in terms of Marcus theory,[27] *i.e.*, taking into account the reorganization energy, see eq 4) between neighboring molecules is analyzed in Figure 5c. We find resonances with average occurrence rates of ~56, ~90, and ~120 THz (18, 11, and 8 fs, respectively),

when computing the resonances between an NPB molecule and its nearest 3, 5, and 7 neighbors.

$$W_{ij} = \frac{2\pi |J_{ij}|^2}{h} \sqrt{\frac{\pi}{\lambda k_B T}} \, e^{-(E_j - E_i + \lambda)^2 / 4\lambda k_B T} \tag{4}$$

To compare these characteristic fluctuation and resonance times to typical hopping rates, we have to take into account the electronic coupling between NPB molecules, which quantifies the prefactor of the Marcus hopping rate and which can be interpreted as a hopping attempt frequency. The electronic coupling strongly depends on the intermolecular distance (see Figure S6). The pair correlation function of NPB (Figure 5a) shows that a substantial amount of NPB molecules have their nearest neighbor at center-of-mass distances between 3 and 8 Å (with a stacking motive in which two NPB molecules are situated in close proximity and rotated approximately 90° relative to each other). The next nearest neighbors that are still in direct contact, thus allowing for nonvanishing electronic coupling matrix elements, are located at distances between 9 and 10 Å.

Electronic couplings J_{ij} and reorganization energies are typically obtained from quantum chemical calculations.[68] For NPB, we obtain $J_{ij} = 0.01$ eV at a distance of ~5 Å and a reorganization energy $\lambda = 0.16$ eV, leading to a maximum hopping rate of 4.2 THz for Marcus theory, assuming that the resonance condition is fulfilled, i.e., for $E_j - E_i + \lambda = 0$. This translates to a residence time $1/W_{ij}$ of 238 fs, which suggests that the oscillations visible in Figure 5b appear averaged for most of the charge carriers. When taking into account larger hopping distances, the mean electronic coupling is substantially lower, allowing the assumption that the energy levels appear time-averaged. This means that the resulting mean energy levels of molecules should be drawn from the static disorder distribution. If we were to remove the distinct oscillations from the frequency spectrum (filter out frequencies higher than 10 THz), then the dynamic disorder would shrink by 22 meV from 84 to 62 meV, but the average resonance occurrence time increases from 11 to 67 fs for 5 neighbors considered.

Nonetheless, we also note that in case of molecules with higher mean electronic couplings than NPB (e.g., J_{ij} of ~0.1 eV, corresponding to a prefactor of the Marcus rate of 418 THz or 2 fs in resonance conditions), even distinct dynamic oscillations become comparable or slower than typical hopping rates, leading to a significantly increased effective disorder experienced by charge carriers in a classical description. Although this is a classical picture and the analogue is not strictly true, the fast distinct oscillations in Figure 5b may be regarded as a way to bring neighboring energy levels into resonance or as phonons being absorbed to facilitate hopping as in Marcus theory. We would like to point out that with an ML model introduced into atomistic charge transport models, these relative contributions could be captured and quantified by introducing the time-dependent energy levels.

For example, a larger grid of realistic time-dependent energy sites could in principle be generated for Monte Carlo simulations. Also, in extensive 3D morphologies, a joint energetic and geometric representation will also reveal possible percolation pathways (see Figure S4). Further properties, like the electronic couplings between two molecules (see Figure S18) and electrostatic effects of charges, can be learned and

added to an ML model. This could be explored in future work, integrating ML models in charge transport simulations.[69−71]

To arrive at a static disorder, which can be used in mesoscopic models, e.g., in kinetic Monte Carlo simulations, the static conformational disorder computed in this work has to be complemented with the electrostatic disorder σ_p, which can be contributed to intermolecular electrostatic interactions, e.g., molecular dipole moments. The electrostatic disorder for the morphologies in this work can be calculated with the QuantumPatch method,[21,34] which yields $\sigma_p = 83$ meV for NPB. Assuming that electrostatic and static conformational disorders are not correlated, the total static disorder is equal to $\sqrt{\sigma_s^2 + \sigma_p^2} = 98$ meV. This is close to the disorder parameter (87 meV) used in mesoscopic models of charge transport[72−74] that is used by a top-down approach to reproduce the experimentally observed hole mobility of NPB. Moreover, the hole mobility of NPB computed with the kMC model with a realistic morphology and assuming a disorder parameter 0.93 eV yields a hole mobility of 2×10^{-3} cm^2/(V s)[75] close to the experimental value (between 2×10^{-3} and 3×10^{-3} cm^2/(V s) according to Chen et al.[76] and Tse et al.[77]). However, a direct comparison with experimental values for the disorder is difficult as most of the measurements are based on the Gaussian disorder model (GDM) or the correlated disorder model (CDM) evaluating the field and temperature dependencies of the mobility and indirectly retrieving the disorder parameter. For small molecules, the measured disorder values will also be composed of contributions of the reorganization energy λ and are not directly comparable with the conformational disorder calculated here. Moreover, the GDM used in experimental work assumes a strictly Gaussian disorder, whereas the simulated static disorder deviates from a Gaussian distribution. With this caveat in mind, we compare the calculated values to a selection of experimental values from the literature in Table S5 and find an overall reasonable agreement. Additionally, we note that the morphologies evaluated in this work are thermodynamically assembled and annealed structures. Distinct (anisotropic) stacking patterns of molecules during film growth influence the effective disorder observed in experiments, which currently cannot be fully observed in simulations. This can potentially explain discrepancies in the predicted disorder of, e.g., B4PyMPM[78,79] (see Table S5).

■ CONCLUSIONS

In summary, we have investigated static and dynamic conformational disorder for various device-relevant organic semiconductors by using machine learning models integrated in multiscale modeling simulations. The ML models were trained using DFT energies to predict the time- and space-resolved energy level distribution of complete MD trajectories of disordered thin films. Thereby, static and dynamic disorder contributions were analyzed using ~38 million energy level predictions by the ML model, a number that would not have been feasible using quantum mechanical calculations.

We first find that static disorder distributions of multiple relevant materials are highly asymmetrical. Consequently, the density of states either shows deep tail states in the HOMO−LUMO gap, which is unfavorable for charge transport (e.g., the HOMO distribution of NPB and TPBi), or it shows a steep decline toward the HOMO−LUMO gap, which avoids trapping and thus favors charge transport (e.g., the HOMO

distribution of Spiro-TAD). We suspect that the underlying mechanism is related to the HOMO energy surface close to the local minima of the potential energy surface. A closer study of this mechanism might lead to new molecular design principles.

Second, we find that characteristic oscillation times of molecular energy levels are below maximally possible Marcus hopping rates in disordered materials like NPB, suggesting that dynamic disorder averages out at typical electronic couplings of disordered materials, leaving static disorder as the key contribution to charge transport. Third, we observed that the amount of static disorder is likely correlated to the size and the amount of rotatable side groups (*e.g.*, TCTA and BPD), provided that the respective molecular energy level is sufficiently delocalized over the molecule and therefore affected by conformational changes. This effect offers the opportunity to be used as a design rule for future organic semiconductors.

In summary, we showed that the integration of ML models as fast and accurate predictors in multiscale modeling workflows offers the opportunity to study a wide range of interesting and application-relevant phenomena, *e.g.*, time-resolved energy level fluctuations, dynamic disorder, and asymmetries in static energy level distributions, which were not accessible before due to prohibitively high computational costs.

ASSOCIATED CONTENT

Supporting Information

The Supporting Information is available free of charge at https://pubs.acs.org/doi/10.1021/acs.jctc.1c00191.

> Tables of machine learning and DFT predictions of conformational disorder for all materials and figures of static and dynamic HOMO/LUMO distribution plotted for all materials, averaged power spectra, electronic couplings for NPB, TCTA orbitals, mass density equilibration, NPB basis set dependence of DFT, 3D static HOMO levels for NPB, and comparison with experiment (PDF)

AUTHOR INFORMATION

Corresponding Author

Pascal Friederich − *Institute of Nanotechnology, Karlsruhe Institute of Technology (KIT), Eggenstein-Leopoldshafen 76344, Germany; Institute of Theoretical Informatics, Karlsruhe Institute of Technology (KIT), Karlsruhe 76131, Germany;* ⬥ orcid.org/0000-0003-4465-1465; Email: pascal.friederich@kit.edu

Authors

Patrick Reiser − *Institute of Nanotechnology, Karlsruhe Institute of Technology (KIT), Eggenstein-Leopoldshafen 76344, Germany; Institute of Theoretical Informatics, Karlsruhe Institute of Technology (KIT), Karlsruhe 76131, Germany;* ⬥ orcid.org/0000-0002-7052-696X

Manuel Konrad − *Institute of Nanotechnology, Karlsruhe Institute of Technology (KIT), Eggenstein-Leopoldshafen 76344, Germany*

Artem Fediai − *Institute of Nanotechnology, Karlsruhe Institute of Technology (KIT), Eggenstein-Leopoldshafen 76344, Germany;* ⬥ orcid.org/0000-0002-4156-115X

Salvador Léon − *Department of Industrial Chemical Engineering and Environment, Universidad Politécnica de Madrid, Madrid 28006, Spain;* ⬥ orcid.org/0000-0002-2757-9417

Wolfgang Wenzel − *Institute of Nanotechnology, Karlsruhe Institute of Technology (KIT), Eggenstein-Leopoldshafen 76344, Germany*

Complete contact information is available at:
https://pubs.acs.org/10.1021/acs.jctc.1c00191

Notes
The authors declare no competing financial interest.

REFERENCES

(1) Geffroy, B.; Le Roy, P.; Prat, C. Organic Light-Emitting Diode (OLED) Technology: Materials, Devices and Display Technologies. *Polym. Int.* **2006**, *55*, 572−582.

(2) Zhang, G.; Zhao, J.; Chow, P. C. Y.; Jiang, K.; Zhang, J.; Zhu, Z.; Zhang, J.; Huang, F.; Yan, H. Nonfullerene Acceptor Molecules for Bulk Heterojunction Organic Solar Cells. *Chem. Rev.* **2018**, *118*, 3447−3507.

(3) Kuehne, A. J. C.; Gather, M. C. Organic Lasers: Recent Developments on Materials, Device Geometries, and Fabrication Techniques. *Chem. Rev.* **2016**, *116*, 12823−12864.

(4) Katz, H. E.; Bao, Z.; Gilat, S. L. Synthetic Chemistry for Ultrapure, Processable, and High-Mobility Organic Transistor Semiconductors. *Acc. Chem. Res.* **2001**, *34*, 359−369.

(5) Diao, Y.; Tee, B. C.-K.; Giri, G.; Xu, J.; Kim, D. H.; Becerril, H. A.; Stoltenberg, R. M.; Lee, T. H.; Xue, G.; Mannsfeld, S. C. B.; Bao, Z. Solution Coating of Large-Area Organic Semiconductor Thin Films with Aligned Single-Crystalline Domains. *Nat. Mater.* **2013**, *12*, 665−671.

(6) Irimia-Vladu, M. "Green" Electronics: Biodegradable and Biocompatible Materials and Devices for Sustainable Future. *Chem. Soc. Rev.* **2014**, *43*, 588−610.

(7) Fediai, A.; Symalla, F.; Friederich, P.; Wenzel, W. Disorder Compensation Controls Doping Efficiency in Organic Semiconductors. *Nat. Commun.* **2019**, *10*, 4547.

(8) Li, J.; Duchemin, I.; Roscioni, O. M.; Friederich, P.; Anderson, M.; Da Como, E.; Kociok-Köhn, G.; Wenzel, W.; Zannoni, C.; Beljonne, D.; Blase, X.; D'Avino, G. Host Dependence of the Electron Affinity of Molecular Dopants. *Mater. Horiz.* **2019**, *6*, 107−114.

(9) Reiser, P.; Müller, L.; Sivanesan, V.; Lovrincic, R.; Barlow, S.; Marder, S. R.; Pucci, A.; Jaegermann, W.; Mankel, E.; Beck, S. Dopant Diffusion in Sequentially Doped Poly(3-Hexylthiophene) Studied by Infrared and Photoelectron Spectroscopy. *J. Phys. Chem. C* **2018**, *122*, 14518−14527.

(10) Tyagi, P.; Tuli, S.; Srivastava, R. Study of Fluorescence Quenching Due to 2, 3, 5, 6-Tetrafluoro-7, 7', 8, 8'-Tetracyano Quinodimethane and Its Solid State Diffusion Analysis Using Photoluminescence Spectroscopy. *J. Chem. Phys.* **2015**, *142*, No. 054707.

(11) Yuan, Y.; Giri, G.; Ayzner, A. L.; Zoombelt, A. P.; Mannsfeld, S. C. B.; Chen, J.; Nordlund, D.; Toney, M. F.; Huang, J.; Bao, Z. Ultra-High Mobility Transparent Organic Thin Film Transistors Grown by an off-Centre Spin-Coating Method. *Nat. Commun.* **2014**, *5*, 3005.

(12) Chu, M.; Fan, J.-X.; Yang, S.; Liu, D.; Ng, C. F.; Dong, H.; Ren, A.-M.; Miao, Q. Halogenated Tetraazapentacenes with Electron Mobility as High as 27.8 Cm2 V^{-1} S^{-1} in Solution-Processed n-Channel Organic Thin-Film Transistors. *Adv. Mater.* **2018**, *30*, 1803467.

(13) Helfrich, W.; Schneider, W. G. Recombination Radiation in Anthracene Crystals. *Phys. Rev. Lett.* **1965**, *14*, 229−231.

(14) Bässler, H. Charge Transport in Disordered Organic Photo-conductors a Monte Carlo Simulation Study. *Phys. Status Solidi B* **1993**, *175*, 15−56.

(15) Bässler, H.; Köhler, A. 7 - Charge Carrier Mobility in Amorphous Organic Semiconductors. In *Organic Light-Emitting Diodes (OLEDs)*; Buckley, A. Ed.; Woodhead Publishing Series in Electronic and Optical Materials; Woodhead Publishing: 2013; pp. 192−234.

(16) Bässler, H.; Köhler, A. Charge Transport in Organic Semiconductors. In *Unimolecular and Supramolecular Electronics I: Chemistry and Physics Meet at Metal-Molecule Interfaces*; Metzger, R. M. Ed.; Topics in Current Chemistry; Springer: Berlin, Heidelberg, 2012; pp. 1−65.

(17) Friederich, P.; Fediai, A.; Kaiser, S.; Konrad, M.; Jung, N.; Wenzel, W. Toward Design of Novel Materials for Organic Electronics. *Adv. Mater.* **2019**, *31*, 1808256.

(18) Friederich, P.; Konrad, M.; Strunk, T.; Wenzel, W. Machine Learning of Correlated Dihedral Potentials for Atomistic Molecular Force Fields. *Sci. Rep.* **2018**, *8*, 2559.

(19) Friederich, P.; Gómez, V.; Sprau, C.; Meded, V.; Strunk, T.; Jenne, M.; Magri, A.; Symalla, F.; Colsmann, A.; Ruben, M.; Wenzel, W. Rational In Silico Design of an Organic Semiconductor with Improved Electron Mobility. *Adv. Mater.* **2017**, *29*, 1703505.

(20) Symalla, F.; Friederich, P.; Massé, A.; Meded, V.; Coehoorn, R.; Bobbert, P.; Wenzel, W. Charge Transport by Superexchange in Molecular Host-Guest Systems. *Phys. Rev. Lett.* **2016**, *117*, 276803.

(21) Friederich, P.; Meded, V.; Symalla, F.; Elstner, M.; Wenzel, W. QM/QM Approach to Model Energy Disorder in Amorphous Organic Semiconductors. *J. Chem. Theory Comput.* **2015**, *11*, 560−567.

(22) Andrienko, D. Multiscale Concepts in Simulations of Organic Semiconductors. In *Handbook of Materials Modeling: Methods: Theory and Modeling*; Andreoni, W.; Yip, S. Eds.; Springer International Publishing: Cham, 2020; pp. 1431−1442.

(23) Fediai, A.; Emering, A.; Symalla, F.; Wenzel, W. Disorder-Driven Doping Activation in Organic Semiconductors. *Phys. Chem. Chem. Phys.* **2020**, *22*, 10256−10264.

(24) Symalla, F.; Fediai, A.; Armleder, J.; Kaiser, S.; Strunk, T.; Neumann, T.; Wenzel, W. 43-3: Ab-Initio Simulation of Doped Injection Layers. In *SID Symposium Digest of Technical Papers*; 2020; *51*, 630−633. DOI: 10.1002/sdtp.13946.

(25) Groves, C. Simulating Charge Transport in Organic Semi-conductors and Devices: A Review. *Rep. Prog. Phys.* **2017**, *80*, No. 026502.

(26) Miller, A.; Abrahams, E. Impurity Conduction at Low Concentrations. *Phys. Rev.* **1960**, *120*, 745−755.

(27) Marcus, R. A. Electron Transfer Reactions in Chemistry. Theory and Experiment. *Rev. Mod. Phys.* **1993**, *65*, 599−610.

(28) Pasveer, W. F.; Cottaar, J.; Tanase, C.; Coehoorn, R.; Bobbert, P. A.; Blom, P. W. M.; de Leeuw, D. M.; Michels, M. A. J. Unified Description of Charge-Carrier Mobilities in Disordered Semi-conducting Polymers. *Phys. Rev. Lett.* **2005**, *94*, 206601.

(29) Bouhassoune, M.; van Mensfoort, S. L. M.; Bobbert, P. A.; Coehoorn, R. Carrier-Density and Field-Dependent Charge-Carrier Mobility in Organic Semiconductors with Correlated Gaussian Disorder. *Org. Electron.* **2009**, *10*, 437−445.

(30) Massé, A.; Friederich, P.; Symalla, F.; Liu, F.; Nitsche, R.; Coehoorn, R.; Wenzel, W.; Bobbert, P. A. *Ab Initio* Charge-Carrier

(31) Kirkpatrick, J.; Marcon, V.; Nelson, J.; Kremer, K.; Andrienko, D. Charge Mobility of Discotic Mesophases: A Multiscale Quantum and Classical Study. *Phys. Rev. Lett.* **2007**, *98*, 227402.

(32) Rodin, V.; Symalla, F.; Meded, V.; Friederich, P.; Danilov, D.; Poschlad, A.; Nelles, G.; von Wrochem, F.; Wenzel, W. Generalized Effective-Medium Model for the Carrier Mobility in Amorphous Organic Semiconductors. *Phys. Rev. B* **2015**, *91*, 155203.

(33) Rühle, V.; Lukyanov, A.; May, F.; Schrader, M.; Vehoff, T.; Kirkpatrick, J.; Baumeier, B.; Andrienko, D. Microscopic Simulations of Charge Transport in Disordered Organic Semiconductors. *J. Chem. Theory Comput.* **2011**, *7*, 3335−3345.

(34) Friederich, P.; Meded, V.; Poschlad, A.; Neumann, T.; Rodin, V.; Stehr, V.; Symalla, F.; Danilov, D.; Lüdemann, G.; Fink, R. F.; Kondov, I.; von Wrochem, F.; Wenzel, W. Molecular Origin of the Charge Carrier Mobility in Small Molecule Organic Semiconductors. *Adv. Funct. Mater.* **2016**, *26*, 5757−5763.

(35) Poelking, C.; Tietze, M.; Elschner, C.; Olthof, S.; Hertel, D.; Baumeier, B.; Würthner, F.; Meerholz, K.; Leo, K.; Andrienko, D. Impact of Mesoscale Order on Open-Circuit Voltage in Organic Solar Cells. *Nat. Mater.* **2015**, *14*, 434−439.

(36) Yavuz, I.; Martin, B. N.; Park, J.; Houk, K. N. Theoretical Study of the Molecular Ordering, Paracrystallinity, And Charge Mobilities of Oligomers in Different Crystalline Phases. *J. Am. Chem. Soc.* **2015**, *137*, 2856−2866.

(37) Hervet, H.; Dianoux, A. J.; Lechner, R. E.; Volino, F. Neutron Scattering Study of Methyl Group Rotation in Solid Para-Azoxyanisole (PAA). *J. Phys.* **1976**, *37*, 587−594.

(38) Harada, J.; Ogawa, K. Invisible but Common Motion in Organic Crystals: A Pedal Motion in Stilbenes and Azobenzenes. *J. Am. Chem. Soc.* **2001**, *123*, 10884−10888.

(39) Llamas-Saiz, A. L.; Foces-Foces, C.; Fontenas, C.; Jagerovic, N.; Elguero, J. The Search for Proton Mobility in Solid Pyrazoles: Molecular and Crystal Structure of 3(5)-Phenyl-4-Bromo-5(3)-Methylpyrazole. *J. Mol. Struct.* **1999**, *484*, 197−205.

(40) White, M. A.; Wasylishen, R. E.; Eaton, P. E.; Xiong, Y.; Pramod, K.; Nodari, N. Orientational Disorder in Solid Cubane: A Thermodynamic and Carbon-13 NMR Study. *J. Phys. Chem.* **1992**, *96*, 421−425.

(41) Cruz-Cabeza, A. J.; Day, G. M.; Jones, W. Structure Prediction, Disorder and Dynamics in a DMSO Solvate of Carbamazepine. *Phys. Chem. Chem. Phys.* **2011**, *13*, 12808−12816.

(42) Richards, T.; Bird, M.; Sirringhaus, H. A Quantitative Analytical Model for Static Dipolar Disorder Broadening of the Density of States at Organic Heterointerfaces. *J. Chem. Phys.* **2008**, *128*, 234905.

(43) Tummala, N. R.; Zheng, Z.; Aziz, S. G.; Coropceanu, V.; Brédas, J.-L. Static and Dynamic Energetic Disorders in the C_{60}, $PC_{61}BM$, C_{70}, and $PC_{71}BM$ Fullerenes. *J. Phys. Chem. Lett.* **2015**, *6*, 3657−3662.

(44) Zheng, Z.; Tummala, N. R.; Wang, T.; Coropceanu, V.; Brédas, J.-L. Charge-Transfer States at Organic−Organic Interfaces: Impact of Static and Dynamic Disorders. *Adv. Energy Mater.* **2019**, *9*, 1803926.

(45) Kupgan, G.; Chen, X.-K.; Brédas, J.-L. Low Energetic Disorder in Small-Molecule Non-Fullerene Electron Acceptors. *ACS Mater. Lett.* **2019**, *1*, 350−353.

(46) Vehoff, T.; Chung, Y. S.; Johnston, K.; Troisi, A.; Yoon, D. Y.; Andrienko, D. Charge Transport in Self-Assembled Semiconducting Organic Layers: Role of Dynamic and Static Disorder. *J. Phys. Chem. C* **2010**, *114*, 10592−10597.

(47) Vehoff, T.; Baumeier, B.; Troisi, A.; Andrienko, D. Charge Transport in Organic Crystals: Role of Disorder and Topological Connectivity. *J. Am. Chem. Soc.* **2010**, *132*, 11702−11708.

(48) McMahon, D. P.; Troisi, A. Organic Semiconductors: Impact of Disorder at Different Timescales. *ChemPhysChem* **2010**, *11*, 2067−2074.

(49) Ishii, H.; Kobayashi, N.; Hirose, K. Carrier Transport Calculations of Organic Semiconductors with Static and Dynamic Disorder. *Jpn. J. Appl. Phys.* **2019**, *58*, 110501.

(50) Rühle, V.; Junghans, C.; Lukyanov, A.; Kremer, K.; Andrienko, D. Versatile Object-Oriented Toolkit for Coarse-Graining Applications. *J. Chem. Theory Comput.* **2009**, *5*, 3211−3223.

(51) Schleder, G. R.; Padilha, A. C. M.; Acosta, C. M.; Costa, M.; Fazzio, A. From DFT to Machine Learning: Recent Approaches to Materials Science−a Review. *J. Phys. Mater.* **2019**, *2*, No. 032001.

(52) Boese, R.; Antipin, M. Y.; Bläser, D.; Lyssenko, K. A. Molecular Crystal Structure of Acetylacetone at 210 and 110 K: Is the Crystal Disorder Static or Dynamic? *J. Phys. Chem. B* **1998**, *102*, 8654−8660.

(53) Troisi, A.; Cheung, D. L. Transition from Dynamic to Static Disorder in One-Dimensional Organic Semiconductors. *J. Chem. Phys.* **2009**, *131*, No. 014703.

(54) Wang, L.; Li, Q.; Shuai, Z.; Chen, L.; Shi, Q. Multiscale Study of Charge Mobility of Organic Semiconductor with Dynamic Disorders. *Phys. Chem. Chem. Phys.* **2010**, *12*, 3309−3314.

(55) Friederich, P.; León, S.; Perea, J. D.; Roch, L. M.; Aspuru-Guzik, A. The Influence of Sorbitol Doping on Aggregation and Electronic Properties of PEDOT:PSS: A Theoretical Study. *Mach. Learn.: Sci. Technol.* **2020**, *2*, No. 01LT01.

(56) de Silva, P.; Van Voorhis, T. QM/MM Study of Static and Dynamic Energetic Disorder in the Emission Layer of an Organic Light-Emitting Diode. *J. Phys. Chem. Lett.* **2018**, *9*, 1329−1334.

(57) Bannwarth, C.; Caldeweyher, E.; Ehlert, S.; Hansen, A.; Pracht, P.; Seibert, J.; Spicher, S.; Grimme, S. Extended Tight-Binding Quantum Chemistry Methods. *WIREs Comput. Mol. Sci.* **2021**, *11*, No. e01493.

(58) Pracht, P.; Bohle, F.; Grimme, S. Automated Exploration of the Low-Energy Chemical Space with Fast Quantum Chemical Methods. *Phys. Chem. Chem. Phys.* **2020**, *22*, 7169−7192.

(59) Grimme, S. Exploration of Chemical Compound, Conformer, and Reaction Space with Meta-Dynamics Simulations Based on Tight-Binding Quantum Chemical Calculations. *J. Chem. Theory Comput.* **2019**, *15*, 2847−2862.

(60) Malde, A. K.; Zuo, L.; Breeze, M.; Stroet, M.; Poger, D.; Nair, P. C.; Oostenbrink, C.; Mark, A. E. An Automated Force Field Topology Builder (ATB) and Repository: Version 1.0. *J. Chem. Theory Comput.* **2011**, *7*, 4026−4037.

(61) Stroet, M.; Caron, B.; Visscher, K. M.; Geerke, D. P.; Malde, A. K.; Mark, A. E. Automated Topology Builder Version 3.0: Prediction of Solvation Free Enthalpies in Water and Hexane. *J. Chem. Theory Comput.* **2018**, *14*, 5834−5845.

(62) Schmid, N.; Eichenberger, A. P.; Choutko, A.; Riniker, S.; Winger, M.; Mark, A. E.; van Gunsteren, W. F. Definition and Testing of the GROMOS Force-Field Versions 54A7 and 54B7. *Eur. Biophys. J.* **2011**, *40*, 843.

(63) Plimpton, S. Fast Parallel Algorithms for Short-Range Molecular Dynamics. *J. Comput. Phys.* **1995**, *117*, 1−19.

(64) Balasubramani, S. G.; Chen, G. P.; Coriani, S.; Diedenhofen, M.; Frank, M. S.; Franzke, Y. J.; Furche, F.; Grotjahn, R.; Harding, M. E.; Hättig, C.; Hellweg, A.; Helmich-Paris, B.; Holzer, C.; Huniar, U.; Kaupp, M.; Marefat Khah, A.; Karbalaei Khani, S.; Müller, T.; Mack, F.; Nguyen, B. D.; Parker, S. M.; Perlt, E.; Rappoport, D.; Reiter, K.; Roy, S.; Rückert, M.; Schmitz, G.; Sierka, M.; Tapavicza, E.; Tew, D. P.; van Wüllen, C.; Voora, V. K.; Weigend, F.; Wodyński, A.; Yu, J. M. TURBOMOLE: Modular Program Suite for Ab Initio Quantum-Chemical and Condensed-Matter Simulations. *J. Chem. Phys.* **2020**, *152*, 184107.

(65) Kim, K.; Jordan, K. D. Comparison of Density Functional and MP2 Calculations on the Water Monomer and Dimer. *J. Phys. Chem.* **1994**, *98*, 10089−10094.

(66) Friederich, P.; Symalla, F.; Meded, V.; Neumann, T.; Wenzel, W. Ab Initio Treatment of Disorder Effects in Amorphous Organic Materials: Toward Parameter Free Materials Simulation. *J. Chem. Theory Comput.* **2014**, *10*, 3720−3725.

(67) Illig, S.; Eggeman, A. S.; Troisi, A.; Jiang, L.; Warwick, C.; Nikolka, M.; Schweicher, G.; Yeates, S. G.; Henri Geerts, Y.; Anthony, J. E.; Sirringhaus, H. Reducing Dynamic Disorder in Small-Molecule Organic Semiconductors by Suppressing Large-Amplitude Thermal Motions. *Nat. Commun.* **2016**, *7*, 10736.

(68) Glaeser, R. M.; Berry, R. S. Mobilities of Electrons and Holes in Organic Molecular Solids. Comparison of Band and Hopping Models. *J. Chem. Phys.* **1966**, *44*, 3797−3810.

(69) Krämer, M.; Dohmen, P. M.; Xie, W.; Holub, D.; Christensen, A. S.; Elstner, M. Charge and Exciton Transfer Simulations Using Machine-Learned Hamiltonians. *J. Chem. Theory Comput.* **2020**, *16*, 4061−4070.

(70) Farahvash, A.; Lee, C.-K.; Sun, Q.; Shi, L.; Willard, A. P. Machine Learning Frenkel Hamiltonian Parameters to Accelerate Simulations of Exciton Dynamics. *J. Chem. Phys.* **2020**, *153*, No. 074111.

(71) Wang, C.-I.; Joanito, I.; Lan, C.-F.; Hsu, C.-P. Artificial Neural Networks for Predicting Charge Transfer Coupling. *J. Chem. Phys.* **2020**, *153*, 214113.

(72) Massé, A.; Friederich, P.; Symalla, F.; Liu, F.; Meded, V.; Coehoorn, R.; Wenzel, W.; Bobbert, P. A. Effects of Energy Correlations and Superexchange on Charge Transport and Exciton Formation in Amorphous Molecular Semiconductors: An *Ab Initio* Study. *Phys. Rev. B* **2017**, *95*, 115204.

(73) Liu, F.; Massé, A.; Friederich, P.; Symalla, F.; Nitsche, R.; Wenzel, W.; Coehoorn, R.; Bobbert, P. A. *Ab Initio* Modeling of Steady-State and Time-Dependent Charge Transport in Hole-Only α-NPD Devices. *Appl. Phys. Lett.* **2016**, *109*, 243301.

(74) de Vries, X.; Friederich, P.; Wenzel, W.; Coehoorn, R.; Bobbert, P. A. Full Quantum Treatment of Charge Dynamics in Amorphous Molecular Semiconductors. *Phys. Rev. B* **2018**, *97*, No. 075203.

(75) Friederich, P.; Fediai, A.; Li, J.; Mondal, A.; Kotadiya, N. B.; Symalla, F.; Wetzelaer, G.-J. A. H.; Andrienko, D.; Blase, X.; Beljonne, D.; Blom, P. W. M.; Brédas, J.-L.; Wenzel, W. The Influence of Impurities on the Charge Carrier Mobility of Small Molecule Organic Semiconductors. *ArXiv190811854 Cond-Mat Phys.* **2020**.

(76) Chen, B.; Lee, C.; Lee, S.; Webb, P.; Chan, Y.; Gambling, W.; Tian, H.; Zhu, W. Improved Time-of-Flight Technique for Measuring Carrier Mobility in Thin Films of Organic Electroluminescent Materials. *Jpn. J. Appl. Phys.* **2000**, *39*, 1190.

(77) Tse, S. C.; Tsang, S. W.; So, S. K. Polymeric Conducting Anode for Small Organic Transporting Molecules in Dark Injection Experiments. *J. Appl. Phys.* **2006**, *100*, No. 063708.

(78) Yokoyama, D.; Sasabe, H.; Furukawa, Y.; Adachi, C.; Kido, J. Molecular Stacking Induced by Intermolecular C−H···N Hydrogen Bonds Leading to High Carrier Mobility in Vacuum-Deposited Organic Films. *Adv. Funct. Mater.* **2011**, *21*, 1375−1382.

(79) Ji, C.-H.; Oh, I.-S.; Oh, S.-Y. Improving the Performance of Organic Solar Cells Using an Electron Transport Layer of B4PyMPM Self-Assembled Nanostructures. *Electron. Mater. Lett.* **2015**, *11*, 795−800.